

COMPUTER VISION METHOD FOR ANALYZING THE OSCILLATION AND DISPLACEMENT OF SPECIMENS DURING MECHANICAL SHOCK TESTS

Patrick Stähli¹, Lorenz Brenner², André Zahnd², Frank Tillenkamp¹

¹ *Zurich University of Applied Sciences (ZHAW), Institute of Energy Systems and Fluid Engineering (IEFE), Technikumstrasse 9, CH-8401 Winterthur;*

² *Federal Department of Defence, Civil Protection and Sport (DDPS), Federal Office for Civil Protection (FOCP), Spiez Laboratory, Austrasse, CH-3700 Spiez.*

Key words:

civil protection, ground shock, computer vision, specimen deflection

ABSTRACT

The Spiez Laboratory tests civil protection components of all types against ground shock on specific shock test facilities. Acceleration sensors and velocity measurements provide hereby information about the displacement by integrating the corresponding signal. Until now, only post-shock functional tests and visual controls are feasible to carry out a subsequent damage analysis. For this reason, a novel computer vision based method is developed in order to capture the whole horizontal shock process which allows the analysis of the specimen oscillation, its deflection as well as the detection of design vulnerabilities.

As an initial task, the existing measurement data acquisition has been synchronized with the newly employed high speed camera system. Following, the latter has been positioned and calibrated in order to carry out first test measurements to register the displacement. Based on the obtained data, it has been decided to develop an individual solution with the help of the OpenCV library and point markers. Hereby, the main procedure is as follows: set up camera, calibrate camera, install test specimen, register camera images during the shock and evaluate camera images. One crucial task is the camera calibration. With the help of a specifically designed calibration target, it was achieved to correct any errors due to the camera optics as well as the perspective of the camera.

Consequently, a method was elaborated to measure the displacements in the measuring plane independently of the camera position. Hereby, different software solutions were programmed for the calibration, measurement and evaluation. By experiments it was shown that the novel measuring system is functional with an accuracy of approximately ± 2 mm.

INTRODUCTION

The Spiez Laboratory maintains a horizontal shock test rig to simulate ground shocks and to monitor the corresponding behaviour of civil protection components. At the current date, investigations base on a qualitative assessment, where the foot point excitation as well as the acceleration is measured on the main test platform. With the increasing interest to obtain detailed information on the structural behaviour in the context of failure or damage analysis as well as to optimize mounting designs, novel measurement techniques are required.

In the last couple of years, several studies applied digital imaging techniques in the context of structures subjected to shock or blast loads in order to measure deformations. Exemplarily, Wang et al. investigated the effects of air-blast loads on composite structures, where high-speed photography together with 3D Digital Image Correlation (DIC) techniques were applied [1]. From the latter, the complete real-time response of the composite materials and the corresponding fluid-structure interaction time was derived. Another study focused on the dynamic response of steel plates when exposed to blast waves with a peak reflected overpressure in a range of approximately 2.7 to 14.5 bar [2]. To measure the transient displacement fields a stereovision camera setup was applied, where an in-house 3D DIC code was used to compare the different deformed configurations with the reference. To facilitate the correlation, a speckle pattern was applied on the investigated specimens. Furthermore, Spranghers et al. investigated the dynamic response of aluminium plates under free air explosions [3]. As large deflections were expected, the aperture of the cameras was reduced, while the illumination was increased to compensate for the latter. To obtain adequate results, a frame rate of 25'000 frames per second (FPS) and a shutter time of 25 μ s was used.

Accordingly, computer vision techniques seem suitable to obtain further information during the shock tests, e.g. to record object deflections. Consequently, the present work introduces an imaging procedure to create time-synchronized video recordings with the existing measurement chain. This allows a follow-up evaluation of eventual design weaknesses of the test specimens. Furthermore, a contactless method is developed to quantitatively determine deflections and natural vibrations of the test objects by applying the OpenCV library [4].

TEST RIG AND HARDWARE

Horizontal shock test rig

Figure 1 depicts the horizontal shock test rig. It consists of a test platform, on which the specimens are mounted, as well as a shock mass weighing about 45 tons. Both platforms are mounted on slightly inclined steel rails and are equipped with a hydraulic braking system. For a shock test, the shock mass is pulled upwards and, subsequently, is released. It then collides inelastically with the test platform, which generates a foot point excitation in the mounted specimen. Ultimately, both platforms are braked until they reach their end position. Depending on the speed of the shock mass, different loads might be generated.

Acceleration measurement

To measure the acceleration and to control the load profile, four unidirectional acceleration sensors of the type Kistler 8203A50 are mounted on the test platform. The acceleration data is registered with a transient recorder of the type Elsys TraNET with a measurement rate of 3 kHz, where 4096 measuring points are acquired with the measurement software Elsys TranAX 4.1 with a pre-trigger of 10 %. The measurement is triggered when a shock intensity dependent acceleration limit is exceeded.

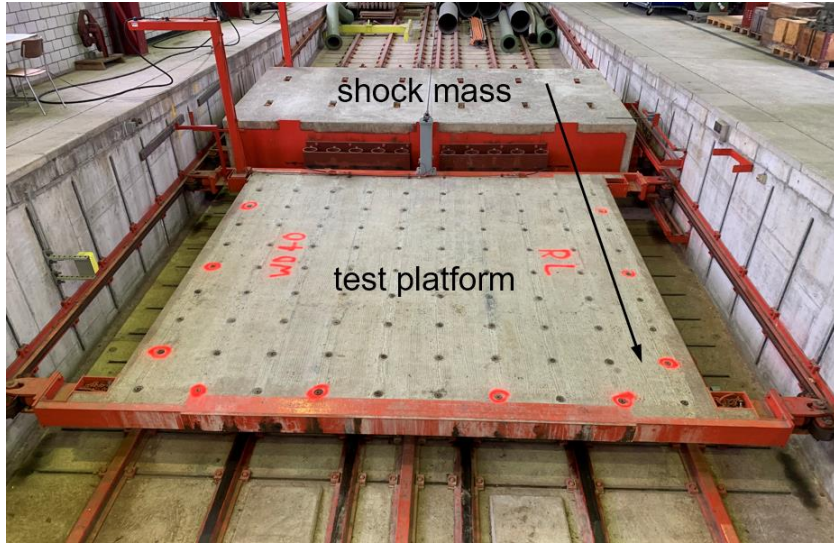


Figure 1: Photograph of the horizontal shock test rig with the shock mass and test table. The arrow indicates the direction of motion.

Camera and lightning systems

For the video capturing a Motion Xtra Os-8 Mono and a Motion Pro Y4 S1 Mono high-speed camera are applied in the present work. Former serves as the master camera to visualize the whole shock, where the latter is applied as the slave camera to determine the specimen deflection in 2D. To achieve an optimum illumination of the test object, two 150 W and one 600 W multi-LED lamps are installed. With an adapter box, the transient recorder triggers the master camera at the same time as the acceleration measurements, where it forwards the signal to the slave camera as well as the LED lamps. The latter are only active during the measurement in order to avoid overheating.

PROCEDURE AND METHODS

Geometrical camera setup

In the present study, a precise alignment of the camera is not necessary because a perspective correction is implemented. However, to keep this correction as small as possible, the camera is positioned approximately perpendicular to the measuring plane. The camera lens is selected in a way that the test specimen remains visible in the image during the entire motion sequence. The section is chosen as narrow as possible in order to reduce the influence of the camera resolution on the accuracy to a minimum. The resulting image section $B_{x,y}$ in x- or y-direction can be determined as follows:

$$B_{x,y} = \frac{d}{f} \cdot S_{x,y} \quad (1)$$

with the sensor size in x- or y-direction $S_{x,y}$, the focus length of the camera lens f and the distance to the measuring plane d (all in millimetres). The approximate resolution of the measuring plane $R_{x,y}$ in x- or y-direction is then obtained with:

$$R_{x,y} = \frac{B_{x,y}}{n_{x,y}} \quad (2)$$

where $n_{x,y}$ represents the number of pixels of the camera sensor in x- or y-direction.

Focus and aperture setup

The camera is focused on the measuring plane and the aperture is closed as far as possible. This assures that the highest possible depth of field is achieved, by still having enough light during short exposure times. The near and far focus plane can be calculated as follows:

$$d_n = \frac{f^2 \cdot d}{f^2 + k \cdot Z \cdot (d - f)} \quad (3)$$

$$d_f = \frac{f^2 \cdot d}{f^2 - k \cdot Z \cdot (d - f)} \quad (4)$$

with the focus length of the camera f , the distance to the measuring plane d , the aperture f-stop number k and the circle of confusion Z . The latter is the diameter of a circle on the camera sensor to which a point source is spread caused by non-perfect focus. It is typically chosen as the size of half a pixel.

Camera calibration and perspective correction

The calibration values of the individual cameras depend, among others, on the selected lens, the focus, the size and the position of the camera sensor. To calibrate a camera, points with known distances relative to each other are detected in various images. This is often realised in the form of a chessboard pattern with a defined field size on a plane, as the individual corners are detected as points very precisely. An extension of this pattern is the so-called ChArUco target, which consists of a chessboard with ArcUco markers in the white fields [5]. The advantage of this pattern is that not only the points are being detected, but are also uniquely recognised with a certain identifier. This allows the application of calibration images on which only parts of the target are visible. In the present work a 0.91 x 1.51 m large ChArUco target with a grid of 12 x 20 fields is applied (see Figure 2). The field and marker size is 70 and 56 mm, respectively, where the Aruco dictionary DICT_4x4_250 is used.

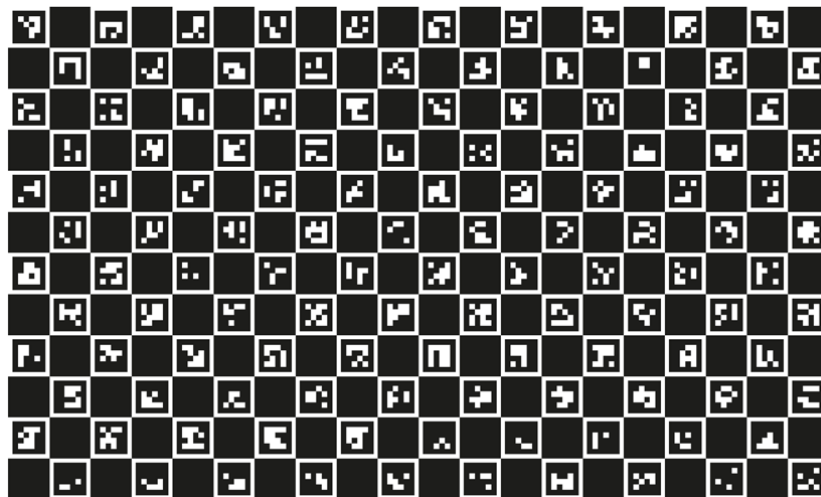


Figure 2: Image of the applied ChArUco pattern for the camera calibration.

First, an intrinsic camera calibration is carried out according to the method of Zhang [6], where the distortion of the optics is corrected. This represents a geometric aberration of optical systems due to the lens shape as well as the imperfectly aligned camera sensor. Such a distortion is for example visible when straight edges reveal a curvature towards the edge of the

image. The intrinsic camera calibration remains valid, as long as no changes are made to the optics, such as changing the focus or aperture settings. The intrinsic camera calibration quality can be quantified by the reprojection error. For this, the checkerboard 3D points are reprojected to the images using the discovered camera calibration parameters. The reprojection error is the RMS distance between the reprojected checkerboard corners and the detected checkerboard corners over all calibration images and is measured in pixels. An acceptable reprojection error is roughly 0.5 pixels or below.

In a second step, an extrinsic camera calibration is performed, where the perspective is corrected. On the one hand, this corrects the fact that the camera is not perpendicular to the measuring plane and, on the other hand, the image is scaled in such a way that a distance of one pixel in the image corresponds to one millimetre. This means that distances can be measured directly in the corrected images, as long as they lie in the measuring plane. The extrinsic camera calibration only remains valid as long as the camera is not moved or rotated and measurements can only be carried out in the chosen measuring plane. Correspondingly, this calibration has to be performed before each test. The extrinsic camera calibration can be qualified by calculating the transformation error. The calibration images used for the extrinsic calibration is transformed using the calculated transformation matrix. In the transformed image, the checkerboard corners are detected again and compared to the known arrangement. The transformation error is the RMS difference between the detected positions and the known positions in millimetres.

Specimen markers

To measure the deflections of the test specimen, circular markers in the measuring plane are required. The position of these markers is later tracked in the video recordings. The markers consist of a white circle on a black background. They must have a diameter of 12 - 19 mm and the distance to the edge must be at least 12 mm. Since the movements relative to the test platform are of particular interest, one marker should be attached as close as possible to the foot point of the specimen and defined as the origin.

Record and evaluate images

The video is recorded and stored with the commercial Software IDT Motion Studio. After the shock test, the first image in the video is loaded and transformed using the calibration data. Subsequently, all circle markers are detected and displayed in the programmed software. One marker is set as the origin, where the others can be chosen individually for the position tracking. Additionally, the origin can be set as fixed according to the first video frame (absolute displacement) or moveable with the other markers (relative displacement). When the tracker is started, the next frame in the video is loaded, transformed and each marker selected for tracking is detected again. To accelerate the process, the search circle is limited to twice the circle marker diameter around the last known position. If a marker cannot be found in 50 consecutive images, it is marked as "lost" and is not tracked any further. The positions of the markers are stored for each frame in the video and displayed in the software.

MEASUREMENT SETUP AND PARAMETERS

In the present study, a three-storey bed deployed in Swiss civil protection shelters is used as the test object (see Figure 3). According to the standardisation, the maximum deflection should be around 100 mm if a ground shock acceleration of 16 g occurs.

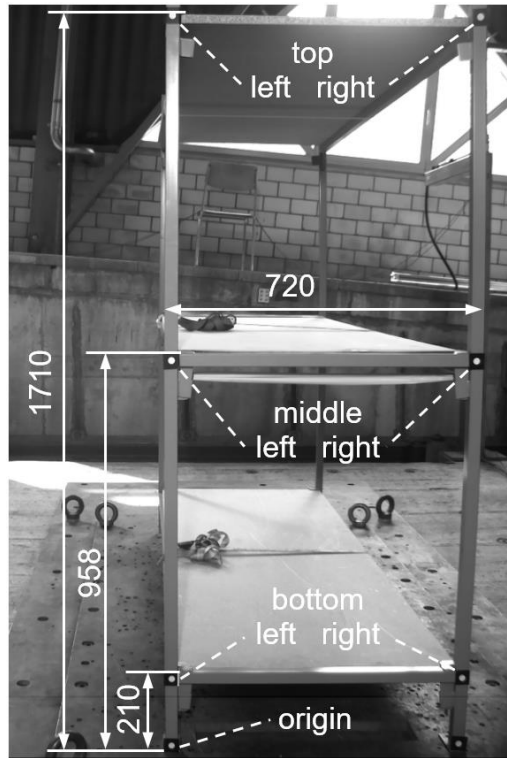


Figure 3: Used test specimen for the experiments with the mounted point markers and the main dimensions in millimetres.

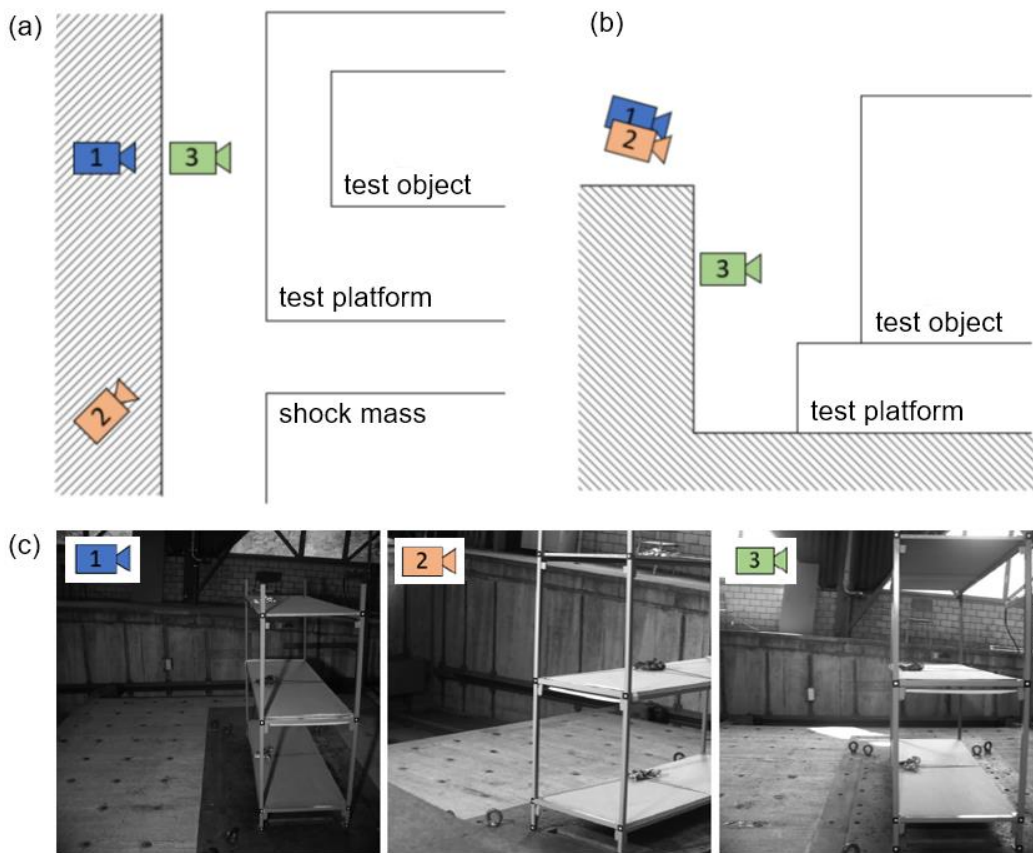


Figure 4: Overview of the different camera positions, top view (a) and side view (b), together with the viewing angle in all positions (c).

To test the developed methodology and to cover a wide range of different viewing angles, three different camera positions are chosen for the measurements (see Figure 4). The corresponding camera and measurement configurations are listed in Table 1.

Table 1: Camera and measurement configuration for each shock.

	Shock 1	Shock 2	Shock 3
Camera position	1	2	3
Camera measurement frequency	1 kHz		
Camera shutter speed	997 μ s		
Camera lens	16 mm	35 mm	16 mm
TraNET measurement frequency	3 kHz		
TraNET measurement samples	4096		
TraNET pre-trigger	10 % (409 samples)		

RESULTS AND DISCUSSION

Geometrical camera setup

Table 2 lists the camera distance to the specimen as well as the applied parameters to compute the image section and resolution for each shock. As expected, the resolution increases with decreasing image section size, since the number of sensor pixels is constant for all camera setups in the present work. The highest resolution of approximately 1.7 mm/px is reached with the camera setup of shock no. 3. If the resolution is insufficient, the distance to the specimen might be reduced or a different camera lens can be applied. Further, it is important to notice, to know the problem to be investigated and to define the hardware as well as the geometric setup in advance in order to obtain the desired image section and resolution.

Table 2: Resulting image sections and resolutions for each camera setup calculated according to Eq. (1) and (2).

	Shock 1	Shock 2	Shock 3
Distance to object (d)	3 m	4.7 m	2 m
Camera lens focal length (f)	16 mm	35 mm	16 mm
Camera sensor size ($S_{x,y}$)	14 x 14 mm		
Image section at d ($B_{x,y}$)	2.6 x 2.6 m	1.9 x 1.9 m	1.7 x 1.7 m
Number of sensor pixels ($n_{x,y}$)	1024 x 1024 px		
Resolution at d ($R_{x,y}$)	2.5 mm/px	1.8 mm/px	1.7 mm/px

Focus and aperture setup

The calculated near and far focus planes with the corresponding parameters for each measurement setup are shown in Table 3. The highest depth of field is achieved with the camera setup for shock no. 1, where the near and far focus plane is in a distance of 1.8 and 8.2 m, respectively. At first glance, this appears to be irrelevant, as measurements are only taken in one plane; however, this plane does not necessarily have to be perpendicular to the camera. Additionally, a large depth of field also simplifies the focusing process.

Table 3: Resulting near and far focus planes for each camera setup calculated according to Eq. (3) and (4).

	Shock 1	Shock 2	Shock 3
Distance to object (d)	3 m	4.7 m	2 m
Camera lens focal length (f)	16 mm	35 mm	16 mm
Aperture f-stop number (k)	8.0	5.6	5.6
Camera sensor pixel size	14 mm / 1024 = 0.0136 mm		
Circle of confusion (Z)	0.0136 mm / 2 = 0.0068 mm		
Near focus plane (d_n)	1.8 m	4.1 m	1.5 m
Far focus plane (d_f)	8.2 m	5.5 m	2.8 m

Camera calibration and perspective correction

For the intrinsic camera calibration, 10 - 20 images of the ChAruCo target are taken from different viewing angles (see Figure 5a). In these images, all visible corner points are detected and their pixel coordinates are stored. Using this positional information and the known specification of the target, the calibration parameters can be determined and later all images can be modified. Consequently, with the proposed method, the distorted images (see Figure 5b) can be successfully corrected (see Figure 5c).

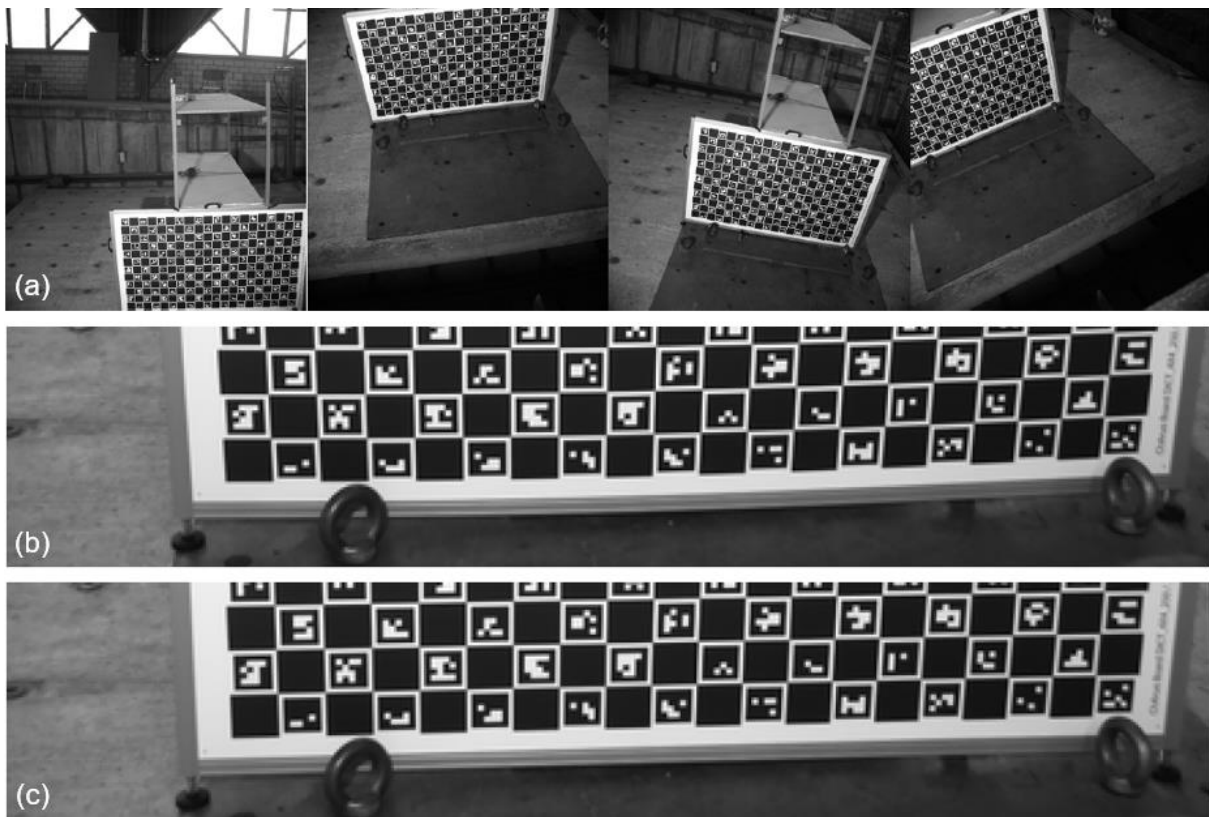


Figure 5: Example of four different calibration images for the intrinsic correction (a). Detail view of the calibration target: uncorrected (b) and corrected image (c).

To correct for camera perspective, the calibration target is placed on the test platform in front of the test object and a calibration image is taken. The printed target surface defines the measurement plane, which is shifted in parallel with an offset equal to the thickness of the target. This ensures that the measurement plane is in line with the front face of the three-storey bed. In addition, the rotational orientation of the target defines the orientation of the coordinate system in the evaluation. In the recorded calibration image, all corner points of the ChArUco target are detected (see Figure 6a) and a transformation matrix is calculated based on the target specifications and the defined offset. The matrix is then applied to correct the perspective and scale the image. This is successfully achieved and it can be observed that the target appears correctly aligned and rotated in the transformed image (see Figure 6b).

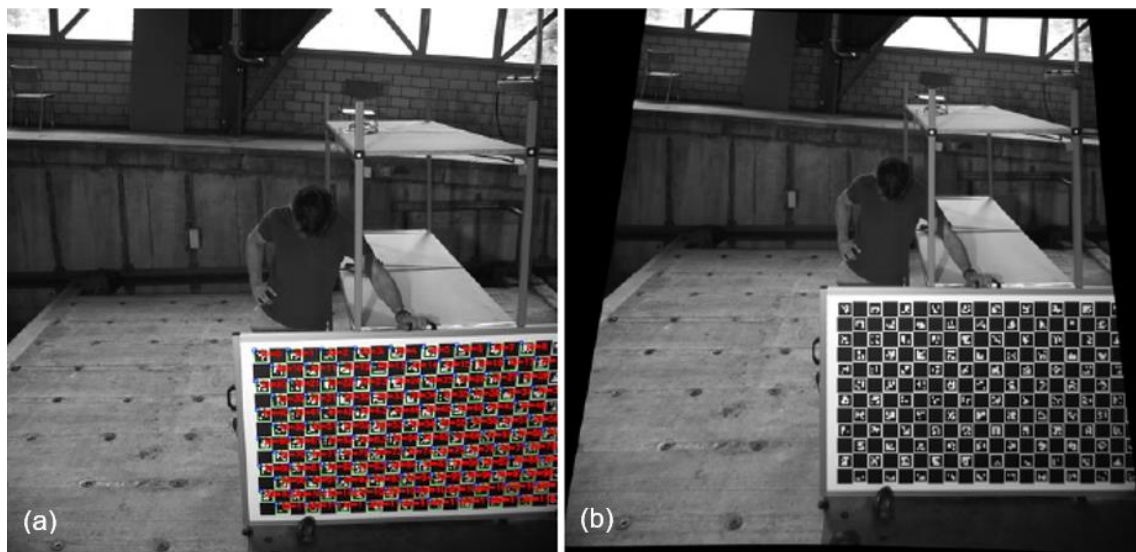


Figure 6: Calibration image with detected points (a) and transformed image (b).

Table 4 lists the reprojection and transformation error of the different camera setups. It is apparent, that the reprojection RMS error is similar for all shocks. Conversely, the camera setup for shock no. 2 reveals a transformation error of 2.25 mm, which is approximately factor 4.5 higher than with the other setups. This is most likely due to the flat viewing angle on the test object, which complicates the perspective correction. Nevertheless, a transformation error of approximately 2 mm is regarded acceptable.

Table 4: Reprojection and transformation root-mean-squared (RMS) error for all applied configurations.



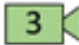
	Shock 1	Shock 2	Shock 3
Reprojection error (RMS)	0.20 pixel	0.23 pixel	0.17 pixel
Transformation error (RMS)	0.45 mm	2.25 mm	0.58 mm

Static measurement and estimation of the accuracy

In order to evaluate the influence of the different camera positions and to estimate the measurement uncertainty of the system, the position of the detected markers is obtained from the first video frame. Accordingly, Table 5 lists all the distances with respect to the origin as

well as the calculated standard deviation. It is observed that similar distances are measured, independently of the three camera angles. One reason for the deviations might be the slight deformation of the test specimen during the performed ground shocks. According to the results, the measurement system correctly detects and measures the positions of the markers with a maximum error of approximately ± 2 mm. In the present work, each frame is evaluated individually. Therefore, the functionality is confirmed and the obtained accuracy is valid for the whole camera registration, i.e. for all subsequent video frames.

Table 5: Measured distances with respect to the origin (compare Figure 3) at the different camera viewing angles in the first video frame.

Marker	Distance to origin in mm			Standard deviation
				
Bottom left	173.4	172.9	173.5	0.3
Bottom right	708.8	708.8	709.6	0.5
Middle left	923.3	921.7	923.0	0.8
Middle right	1146.0	1146.4	1147.0	0.5
Top left	1676.3	1674.8	1675.8	0.8
Top right	1805.9	1803.8	1807.7	1.8
Average standard deviation				0.8

Dynamic measurement

Figure 7a depicts the measured acceleration (y-axis) in function of the time (x-axis) of the different shocks. In all cases, the peak acceleration is reached after approximately 5 ms, where a maximum acceleration of -20 g is achieved with shock no. 2. Ground shock no. 1 and 3 reveal a 20 and 30 % lower peak acceleration, respectively. Starting from 15 ms, the test platform reveals the same behaviour for all shocks. An exception is shock no. 1, where still a positive acceleration of approximately 2 g is measured during the whole registration period. The reason for the latter might be a sensor issue or a delayed breaking of the test platform.

The absolute movement of the test specimen (y-axis) in function of the time (x-axis) during the whole shock process is shown in Figure 7b. With ground shock no. 3 the specimen exhibits the lowest absolute displacement of approximately 165 mm, which is consistent with the acceleration measurement. With shock no. 1 and 2 a total displacement of 290 and 325 mm is revealed, where the movement ends at approximately 450 ms.

Figure 7c illustrates the relative movement of the left top and middle point markers (y-axis) in function of the time (x-axis) for all ground shocks. The test object oscillates at each shock with the same frequency of approximately 2 Hz, where a slight phase shift of 25 ms is observed. Interestingly, the three-storey bed reveals the lowest initial deflection of ca. -50 mm at shock no. 3 (as expected according to the measured peak acceleration) but then exhibits the largest movement amplitudes in comparison to the other shocks. Ultimately, the reason for this behaviour cannot be determined, whereby one possible reason could be a structural change or damage of the specimen due to the previous loads. As expected, the top markers reveal an approximately 50 % larger deflection in comparison to the middle markers due to the present specimen construction. Furthermore, a peak deflection of 100 mm is reached with shock no. 1 (peak acceleration of 16 g), which is consistent with the standardisation value of the investigated three-storey bed for Swiss civil shelters.

Finally, it can be stated, that the measurement system is also functional to analyse dynamic effects and deflections due to simulated ground shocks.

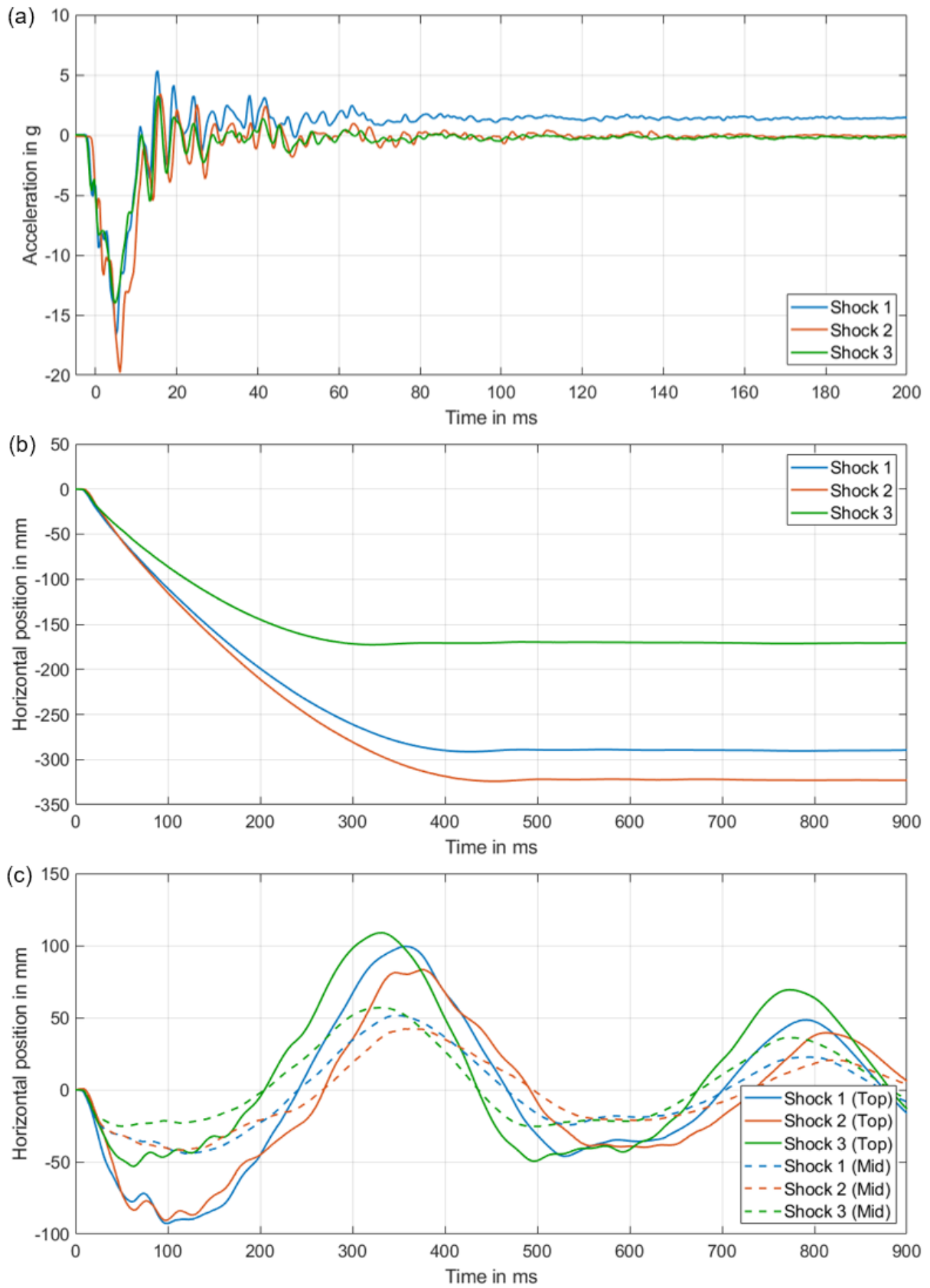


Figure 7: Results of the dynamic measurement during the ground shocks: test platform acceleration (a), absolute movement of the origin marker on the specimen (b) and relative movement of the left top and middle point markers on the specimen (c).

CONCLUSION AND OUTLOOK

This paper presents a computer vision procedure for measuring the deflection of specimens during ground shocks generated on a specific test rig. This comprises the camera setup and its calibration, the video recording as well as the subsequent evaluation. The obtained data revealed that the measurement system is functional independently of the camera viewing angle, where an uncertainty in the measured deflection of approximately ± 2 mm is expected.

Future work will cover the elaboration of a specific software which combines all the presented calibration, measurement and evaluation steps. Furthermore, the method could be extended to not only measure the deflection, but also the occurring stresses at the specimen with additional sensors, e.g. strain gauges. The latter is however regarded as challenging.

ACKNOWLEDGEMENTS

Many thanks go to Rudolf Greub for the support during the shock experiments.

REFERENCES

- [1] E. Wang et al., "Fluid-structure interaction and its effect on the performance of composite structures under air-blast loading," *International Journal of Multiphysics*, vol. 6, no. 3, pp. 219-239, 2012.
- [2] V. Aune et al., "Fluid-structure interaction effects during the dynamic response of clamped thin steel plates exposed to blast loading," *International Journal of Mechanical Sciences*, p. 106263, 2021.
- [3] K. Spranghers et al., "Numerical simulation and experimental validation of the dynamic response of aluminium plates under free air explosion," *International Journal of Impact Engineering*, pp. 83-95, 2013.
- [4] G. Bradski, "The OpenCV Library," *Dr. Dobb's Journal of Software Tools*, vol. 25, no. 11, pp. 120-125, 2000.
- [5] S. Garrido-Jurado et al., "Automatic generation and detection of highly reliable fiducial markers under occlusion," *Pattern Recognition*, vol. 47, no. 6, pp. 2280-2292, 2014.
- [6] Z. Zhang, "A flexible new technique for camera calibration," *IEEE Transactions on Pattern Analysis and Machine Intelligence*, vol. 22, no. 11, pp. 1330 - 1334, 2000.